

Effective Window Function for Lagrangian Halos

Kwan Chuen Chan^{(1,2,3)*}, Ravi K. Sheth⁽⁴⁾, and Román Scoccimarro⁽⁵⁾

¹ *Département de Physique Théorique and Center for Astroparticle Physics, Université de Genève, 24 quai Ernest Ansermet, CH-1211 Genève 4, Switzerland*

² *Institute of Space Sciences, IEEC-CSIC, Campus UAB, Carrer de Can Magrans, s/n, 08193 Bellaterra, Barcelona, Spain*

³ *School of Physics and Astronomy, Sun Yat-Sen University, Guangzhou 510275, China*

⁴ *Center for Particle Cosmology, University of Pennsylvania, 209 S. 33rd St., Philadelphia 19104, Pennsylvania, USA and*

⁵ *Center for Cosmology and Particle Physics, Department of Physics, New York University, New York 10003, New York, USA*

(Dated: October 9, 2018)

The window function for protohalos in Lagrangian space is often assumed to be a tophat in real space. We measure this profile directly and find that it is more extended than a tophat but less extended than a Gaussian; its shape is well-described by rounding the edges of the tophat by convolution with a Gaussian that has a scale length about 5 times smaller. This effective window W_{eff} is particularly simple in Fourier space, and has an analytic form in real space. Together with the excursion set bias parameters, W_{eff} describes the scale-dependence of the Lagrangian halo-matter cross correlation up to $kR_{\text{Lag}} \sim 10$, where R_{Lag} is the Lagrangian size of the protohalo. Moreover, with this W_{eff} , all the spectral moments of the power spectrum are finite, allowing a straightforward estimate of the excursion set peak mass function. This estimate requires a prescription of the critical overdensity enclosed within a protohalo if it is to collapse, which we calibrate from simulations. We find that the resulting estimate of halo abundances is only accurate to about 20%, and we discuss why: A tophat in ‘infall time’ towards the protohalo center need not correspond to a tophat in the initial spatial distribution, so models in which infall rather than smoothed overdensity is the relevant variable may be more accurate.

I. INTRODUCTION

The abundance and clustering of virialized dark matter halos can be used to constrain cosmological parameters [1, 2]. The most widely studied models for halos in the late time Eulerian field are said to be Lagrangian: one postulates that the physics of Eulerian halo formation may be understood by studying the Lagrangian protohalo patches from which they formed. The reason for doing this is that statistics in the Lagrangian space are simpler than in Eulerian space: this is especially true if the initial field is Gaussian. However, defining the protohalos theoretically becomes a non-trivial task. One has to determine what conditions must be satisfied for a Lagrangian patch to form a halo.

In the excursion set approach [3, 4] the Lagrangian protohalo patches from which halos later form are modeled by requiring that the smoothed dark matter density field satisfy certain constraints. This is also true for more elaborate models based on peaks [5–10], and excursion set peaks [11–14]. The smoothing window is often assumed to be a tophat in real space, based on physical grounds. E.g., the spherical collapse model is explicitly about tophat spherical shells: the evolution of a shell is governed by the mean tophat overdensity within it [15–17]. The tophat assumption has the added simplicity that the tophat profile is maintained during collapse, until the

final violent relaxation phase [18].

However, there are scattered hints from previous numerical studies that the Lagrangian shape is more extended than a tophat [19–25]. Moreover, the peaks-based predictions for halo abundance and formation require integrals (over the initial power spectrum), some of which are ill-defined for a tophat window. To alleviate this problem, it is common to use a Gaussian window instead [5], or to use a tophat when it leads to convergent results and a Gaussian otherwise [e.g. 13, 14, 26]. Finding a better motivated, less ad hoc treatment is desirable.

In these approaches, the window function affects both the predicted abundance of halos, as well as their clustering. On large scales, the clustering of halos is linearly biased with respect to the matter. As measurements and theoretical predictions become more precise, it has become necessary to account for the fact that this bias may be scale dependent [see 27, for a recent review]. Correctly modeling this scale dependence requires a good understanding of the window function [5, 28, 29]. Thus, both when predicting halo abundances and when modeling halo bias, the shape of the window function plays a crucial role. The main goal of the present study is to use numerical simulations to determine this shape.

In Sec. II, we describe real-space estimates of the effective window W_{eff} from simulations, and propose a simple analytic parametrization of it. Fourier space estimates are the subject of Sec. II C. In Sec. III, we combine W_{eff} with the collapse threshold measured directly in simulations to see if the excursion set peak approach correctly predicts the halo mass function. We conclude in Sec. IV.

*Electronic address: chan@ice.cat

Several details are provided in Appendices. Appendix A describes a number of systematics: discreteness effects, estimating W_{eff} from a clustered field rather than the initial Lagrangian grid, and the effect of fixing some parameters when fitting the protohalo-matter cross parameter. Dependence on how the halos were defined in the first place is studied in Appendix B. Appendix C discusses how W_{eff} can be understood in the context of the spherical collapse model.

II. LAGRANGIAN WINDOW FUNCTION

Suppose that one has identified halos in the late time Eulerian field. Then, using the initial positions of the particles, one defines the Lagrangian protohalo patch as the region from which each Eulerian halo forms. In Lagrangian models for halos, one postulates that the physics of Eulerian halo formation may be understood by studying the Lagrangian protohalos. The reason for doing this is that statistics in the Lagrangian space are simpler than that in Eulerian space: this is especially true if the initial field is Gaussian. The cost – there is always a price to pay – is the complexity required to define a protohalo in Lagrangian space (the definition is usually relatively simple in Eulerian space). E.g., are protohalos peaks in density? If so on what scale? Is density the only variable which matters? Etc.

In this work, we use two sets of simulations from the LasDamas project: Oriana and Carmen. Both simulation sets assume the same flat Λ CDM model with cosmological parameters $\Omega_m = 0.25$, $\Omega_\Lambda = 0.75$ and $\sigma_8 = 0.8$. The transfer function is taken from CMBFAST [30]. The initial conditions are Gaussian with spectral index $n_s = 1$. The initial particle displacement fields are set using 2LPT [31] at $z_* = 49$, after which the particles are evolved using the public code Gadget2 [32]. In the Oriana simulations, there are 1280^3 particles in a cubic box of size $2400 h^{-1}\text{Mpc}$, and 1120^3 particles in a box of size $1000 h^{-1}\text{Mpc}$ in the Carmen simulations. Thus, in the Oriana and Carmen simulations, each particle carries a mass of 4.57×10^{11} and $4.94 \times 10^{10} h^{-1} M_\odot$ respectively. Our results are averaged over 5 realizations for Oriana, and 7 for Carmen. In each simulation, the Eulerian halos are identified at $z = 0.97$ and $z = 0$ using the Friends-Of-Friends algorithm [33, hereafter FOF] with linking length $\ell = 0.156$ times the interparticle separation. We show results for $\ell = 0.2$ in Appendix B 1. To resolve the halo profiles well, we only consider halos with at least 60 particles; we discuss discreteness effects in Appendix A 1. We bin the halos into narrow mass bins of width $\Delta \ln M = 0.157$.

For each Eulerian halo identified at redshift z (typically $z = 0$ and 0.97 in this paper) we trace back its constituent particles to the initial redshift z_* . The center of mass of the corresponding Lagrangian protohalo is estimated using the center of mass of the constituent particles in the initial Lagrangian space. If the protohalo patches were spherical, then the range of masses in

a bin corresponds to a range of $\sim 5\%$ in Lagrangian radii. This is sufficiently small that we do not expect the results which follow to be affected by the binning.

A. The Lagrangian window in real space

We expect the window function \mathcal{W} to have a number of properties. First, to define a halo in Lagrangian space, we expect it to be compact and reasonably well localized in real space. We use R to denote the ‘scale’ of the filter, where

$$\int d\mathbf{x} \mathcal{W}_R(\mathbf{x}) \equiv V_R \propto R^3. \quad (1)$$

(i.e. \mathcal{W}_R is normalized such that $\mathcal{W}_R(0) = 1$). Although we know that halos, and the protohalo patches from which they formed, are not really spherical [e.g. 22, 34], we will assume, for simplicity, that \mathcal{W} is spherically symmetric. With these minimal conditions, we now describe how we reconstruct the effective window function from the Lagrangian halo profile.

Consider a protohalo centered at the origin. The total number of particles in this halo, N , is given by

$$N = \int d\mathbf{x} n_h(\mathbf{x}) = \int dr 4\pi r^2 n_m(r) p_h(r), \quad (2)$$

where n_m is the number density of dark matter particles, and p_h is the probability that a dark matter particle at distance r from the protohalo center is part of the protohalo. This shows that we can estimate $p_h(r)$ for each protohalo from the ratio $n_h(r)/n_m(r)$, where $n_h(r)$ is the number density of particles belonging to the protohalo that are at distance r from the protohalo center. When the dark matter particle distribution is uniform, as it is in the initial conditions, and discreteness effects are not a concern, then $n_m(r) = \bar{n}_m$ and so $N = \bar{n}_m V_R$.

Even when the Lagrangian halo profile is not tophat, it is convenient to define the Lagrangian radius R_{Lag} from

$$N \equiv \frac{4\pi}{3} \bar{n}_m R_{\text{Lag}}^3, \quad (3)$$

where \bar{n}_m is the mean density of dark matter particles. Then Eq. (1) indicates that we should define

$$\frac{\mathcal{W}(r)}{V_R} \equiv \frac{3 p_h(r)}{4\pi R_{\text{Lag}}^3} \frac{n_m(r)}{\bar{n}_m}. \quad (4)$$

For the rest of the paper, we follow the convention of [5] and use $W \equiv \mathcal{W}/V_R$, which is of dimension $1/\text{Volume}$ in real space and dimensionless in Fourier space. In the initial conditions, $W(r) = p_h(r)/(4\pi R_{\text{Lag}}^3/3)$. This shows that $p(r)$ is proportional to the shape of the window.

We estimate $p_h(r)$ for each protohalo from the ratio $n_h(r)/n_m(r)$, where $n_h(r)$ is the number density of particles belonging to the Lagrangian halo. The results are shown in Fig. 1. To estimate $n_h(r)$, for each Lagrangian

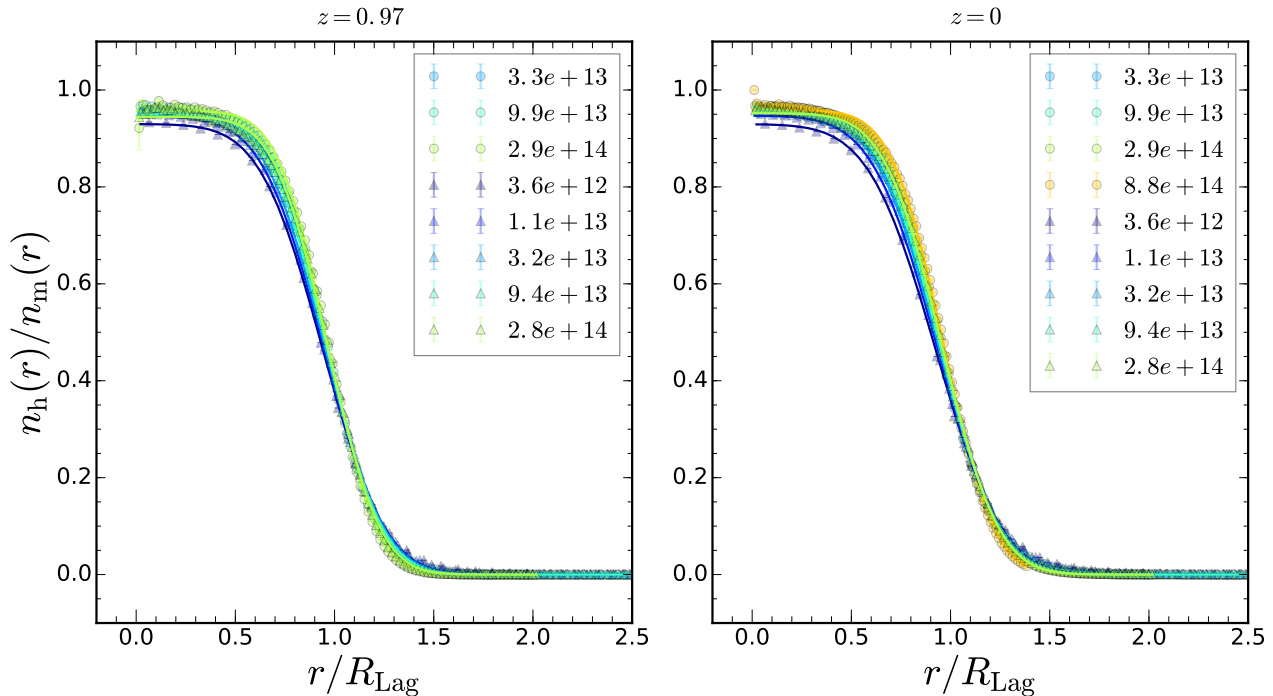


FIG. 1: The estimator n_h/n_m for p_h in Oriana (circles) and Carmen (triangles) for the range of halo masses shown in the legend (in units of $h^{-1}M_\odot$). Solid lines, same color as the symbols, show the result of fitting Eq. (8) to the measurements.

halo, we bin all the protohalo particles belonging to the Lagrangian halo into spherical shells about the center of mass of the halo, and we then compute the number density in each shell. The spherically averaged number density is further averaged over all the halos in the same mass bin. We estimate $n_m(r)$ by carrying out the same procedure for all the particles (protohalo or not). In both cases, we use the particles traced back to the initial grid points, and not the 2LPT displaced positions. See Appendix A 2 for results based on the 2LPT positions.

Fig. 1 shows the measurements from both Carmen and Oriana for the Lagrangian protohalos of Eulerian halos identified at $z = 0.97$ and 0 respectively. The results from the two redshifts are very similar. Normalizing distances by the mean R_{Lag} in the mass bin (rather than doing this halo by halo) removes most of the dependence on mass. Indeed, in this normalized variable, protohalos spanning three orders of magnitude in mass follow very similar profiles. However, there is a small residual mass dependence: the less massive protohalos are slightly more diffuse than the more massive ones. In general, $p_h \sim 1$ on small scales, but when $r/R_{\text{Lag}} \geq 1$, then the profile drops sharply: it is smoother than a tophat and more localized than a Gaussian, in qualitative agreement with Fig. 3 of [20].

The careful reader will have noted that p_h differs from unity at small r . Appendix A 1 discusses this limit and shows that some of the difference from unity is a consequence of discreteness effects, especially for the least

massive halos. Moreover, if the protohalo consists of more than one lump, and we use only the main lump in the Lagrangian protohalo as in [22], the resultant p_h near the center is closer to unity. Thus, while it is possible that a small fraction of particles from the center of the protohalo escape, this fraction is smaller than the Figure indicates.

B. Fitting function for the Lagrangian window

We noted above that $p_h(r)$ is proportional to a smoothing window. For a generic smoothing window, the value of the smoothed overdensity fluctuation field at position \mathbf{x} is

$$\begin{aligned} \delta_W(\mathbf{x}) &= \int d\mathbf{x}' W(\mathbf{x} - \mathbf{x}') \delta_m(\mathbf{x}') \\ &= \frac{1}{\bar{n}_m} \int d\mathbf{x}' W(\mathbf{x} - \mathbf{x}') n_m(\mathbf{x}') - 1. \end{aligned} \quad (5)$$

This shows that, when the position \mathbf{x} corresponds to a protohalo center, then $\delta_W(\mathbf{x})$ is the matter overdensity smoothed with $W \propto p_h(r)$. Fig. 1 shows that W is rather different from (it has rounder edges than) a tophat.

Consider a tophat of radius R_{Lag} centered on a protohalo patch. There are at least three reasons why we expect W to differ from this tophat. First, the protohalos are not spherical, so assuming spherical symmetry can make $p \neq 1$. [34] shows that this matters, but

is a small effect. Second, particles within R_{Lag} having velocities larger than the escape speed will escape (i.e. move beyond R_{Lag}); others which were initially beyond R_{Lag} may have had velocities which brought them closer. Appendix C 2 discusses why both types of particles will tend to smear out the sharp edge. And third, the center of mass of the protohalo patch may be a good but not perfect indicator of the position around which the main collapse occurs; if so, then using it will provide a slightly smeared-out version of the ‘true’ position of the protohalo, and hence of the true p_h shape.

The discussion above motivates us to consider a composite window consisting of a tophat smoothed by a Gaussian. I.e., we define

$$W_{\text{eff}}(kR_{\text{Lag}}) \equiv W_{\text{TH}}(kR_{\text{Lag}}) W_{\text{G}}\left(\frac{kR_{\text{Lag}}}{\phi}\right), \quad (6)$$

where

$$W_{\text{TH}}(x) \equiv \frac{3}{x^3}(\sin x - x \cos x) \text{ and } W_{\text{G}}(x) \equiv e^{-x^2/2} \quad (7)$$

and $\phi \equiv 5/\sqrt{f}$, where the factor of 5 is because, as we will see shortly, the scale of the Gaussian window is about 1/5 of the size of the tophat (R_{Lag}); in turn, this happens to be approximately the same as the Eulerian scale. The parameter f quantifies how the scale of W_{G} differs from $R_{\text{Lag}}/5$: in particular, $W_{\text{eff}} \rightarrow W_{\text{TH}}$ as $f \rightarrow 0$ whereas $W_{\text{eff}} \rightarrow W_{\text{G}}$ as $f \rightarrow \infty$. I.e., larger f values imply more smearing-out.

One of the virtues of this functional form is that its inverse Fourier transform is analytic. The effective window in real space is

$$W_{\text{eff}}(r) = \frac{W_{\text{eff}}(r)}{V_{\text{eff}}} = \frac{3}{4\pi R_{\text{Lag}}^3} \left[\frac{e^{-x_+^2} - e^{-x_-^2}}{\phi x \sqrt{2\pi}} + \frac{\text{erf}(x_+)}{2} - \frac{\text{erf}(|x_-|)}{2} \frac{x_-}{|x_-|} \right], \quad (8)$$

where

$$x \equiv \frac{r}{R_{\text{Lag}}}, \quad x_{\pm} \equiv \frac{\phi(x \pm 1)}{\sqrt{2}}, \quad \phi \equiv \frac{5}{\sqrt{f}}, \quad (9)$$

and

$$V_{\text{eff}} = V_{\text{TH}} \left[\text{erf}\left(\frac{\phi}{\sqrt{2}}\right) - 2\phi \frac{e^{-\phi^2/2}}{\sqrt{2\pi}} \right]^{-1}. \quad (10)$$

Note that V_{eff} interpolates between $V_{\text{TH}} \equiv 4\pi R_{\text{Lag}}^3/3$ when $f \ll 1$ and grows to $V_{\text{G}} \equiv (2\pi f)^{3/2} (R_{\text{TH}}/5)^3$ when $f \gg 1$. If $f < 2$ ($f < 4$), then V_{eff} is one (ten) percent larger than V_{TH} . This will be important in what follows.

When fitting Eq. (8) to the data in Fig. 1 we replace $R_{\text{Lag}} \rightarrow \rho R_{\text{Lag}}$, and allow ρ and f to vary. In addition, we multiply the expression above by an overall amplitude A , which we also allow to vary. Fig. 2 shows the best fit

parameters. We expect ρ and A to be close to unity for all masses, and Fig. 2 shows that this is indeed the case. On the other hand, f is a stronger function of halo mass: it is larger than unity – meaning that the edges of the tophat are more rounded – at small masses, and decreases at large masses. This mass-dependence is different for the two redshifts we have studied, but the redshift dependence is reduced significantly if we express the masses and redshifts in terms of the scaled variable

$$\nu_{\text{sc}} \equiv \frac{\delta_{\text{sc}}(z)}{\sigma_0(M)}, \quad (11)$$

where $\delta_{\text{sc}}(z)$ is the time-dependent spherical collapse threshold and $\sigma_0(M)$ is defined in Eq. (16). When this is done, we find that when $\nu_{\text{sc}} \gtrsim 3$, the best fit f is close to 1, but it increases as ν_{sc} decreases. Appendix A 3 shows that a Fourier space analysis returns similar results. That f depends on ν_{sc} rather than mass suggests that discreteness effects (which scale with particle number) are unlikely to be the dominant cause of the smearing-out we see in Fig. 1.

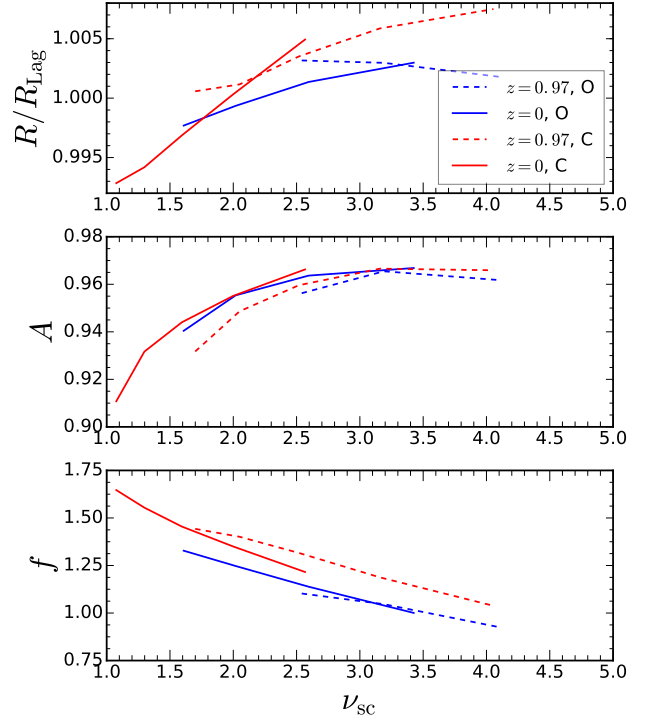


FIG. 2: The best-fit parameters ρ , A and f for the Lagrangian protohalos of halos identified at $z = 0.97$ (dashed) and 0 (solid) in Oriana (blue) and Carmen (red).

C. Fourier space estimate of the window

We now focus on the cross correlation between the protohalo centers and the dark matter; we will not consider

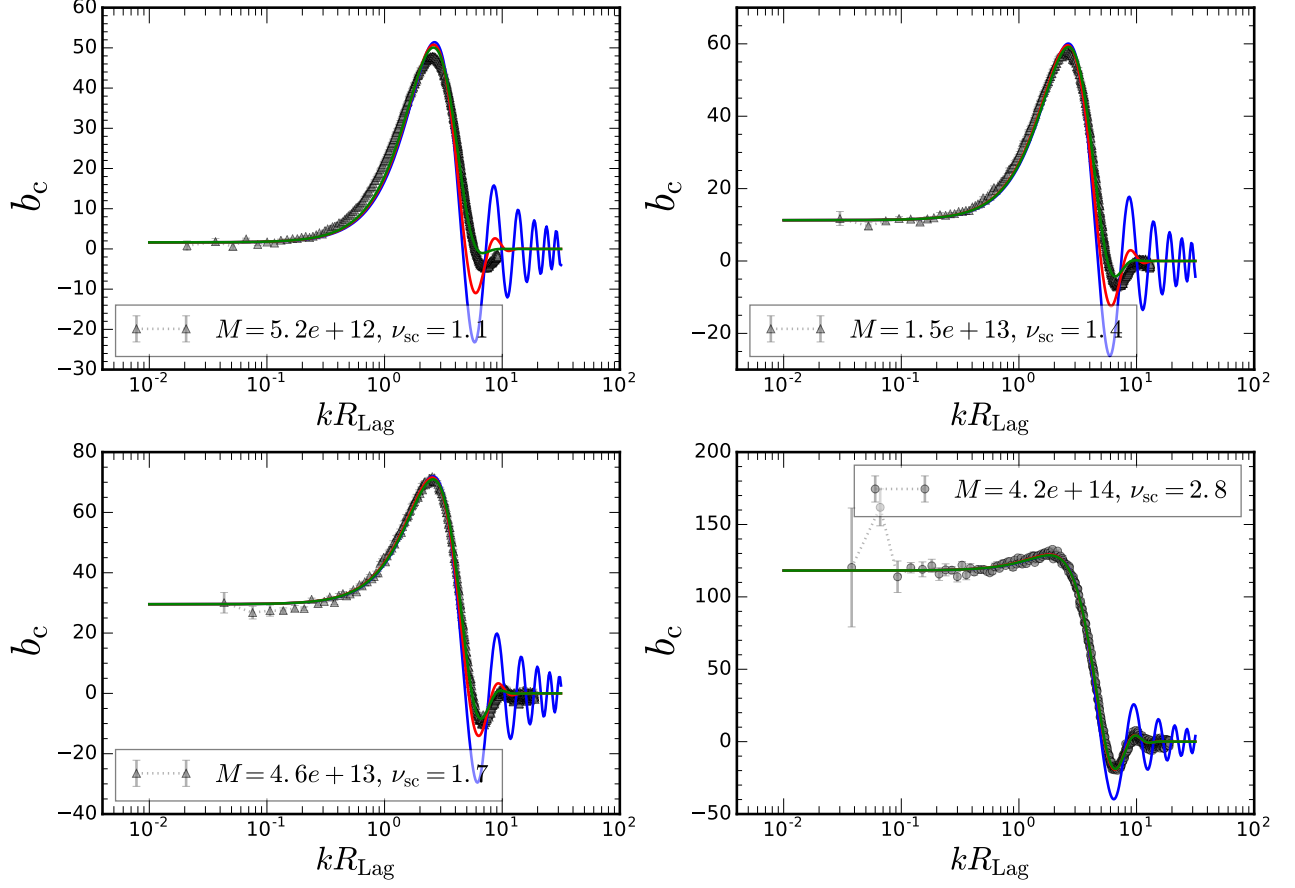


FIG. 3: Lagrangian cross bias parameter b_c for the Lagrangian protohalos of Eulerian halos identified at $z = 0$ in the Oriona (grey circles) and Carmen (grey triangles) simulations, for a range of halo masses (legend, in units of $h^{-1}M_\odot$). Curves show the result of fitting Eq. (15) to these measurements with $W = W_{\text{TH}}$ (blue) and W_{eff} (red), when b_{10} , b_{01} , and R are varied and $f = 1$. Green shows W_{eff} when f is also varied. In some cases, the green and red curves overlap (e.g., when $\nu_{\text{sc}} = 2.8$).

the auto-correlation. In Fourier space, the cross power spectrum between the Lagrangian halo density contrast, δ_h , and that of the dark matter at the initial time, δ_m , is

$$\langle \delta_h(\mathbf{k}_1) \delta_m(\mathbf{k}_2) \rangle = (2\pi)^3 P_c(k_1) \delta_D(\mathbf{k}_{12}), \quad (12)$$

where δ_D is the Dirac delta function. Similarly, the Lagrangian matter power spectrum is defined as

$$\langle \delta_m(\mathbf{k}_1) \delta_m(\mathbf{k}_2) \rangle = (2\pi)^3 P_m(k_1) \delta_D(\mathbf{k}_{12}). \quad (13)$$

In what follows, δ_m is taken from the initial Gaussian random fluctuation field. We discuss the differences when the evolved 2LPT field is used in Appendix A 2.

The halo-matter cross-correlation function is related to the auto-correlation of the dark matter by a single multiplicative (possibly scale-dependent) bias factor [35]. We estimate this Lagrangian cross bias parameter as

$$b_c(k, z) = \frac{D(z_*)}{D(0)} \left[\frac{P_c(k, z_*)}{P_m(k, z_*)} - 1 \right], \quad (14)$$

where we extrapolate the Lagrangian bias parameter to $z = 0$ using the linear growth factor D . We have included the term -1 because of the initial redshift of the simulation is finite (e.g. [36]). The argument z denotes the redshift at which the Eulerian halos were identified.

Fig. 3 shows our measurements of b_c (the right hand side of Eq. (14)) for the protohalo patches of halos identified at $z = 0$ for a range of halo masses (as labelled in each panel). Plotting b_c versus kR_{Lag} rather than k alone removes some of the dependence on mass. For $kR_{\text{Lag}} \lesssim 1$, this quantity approaches a (mass-dependent) constant; it rises to a maximum at $kR_{\text{Lag}} \sim 1$, after which it drops sharply and oscillates with diminishing amplitude as kR_{Lag} increases. We will see shortly that these oscillations have an important implication.

In the excursion set approach, the Lagrangian

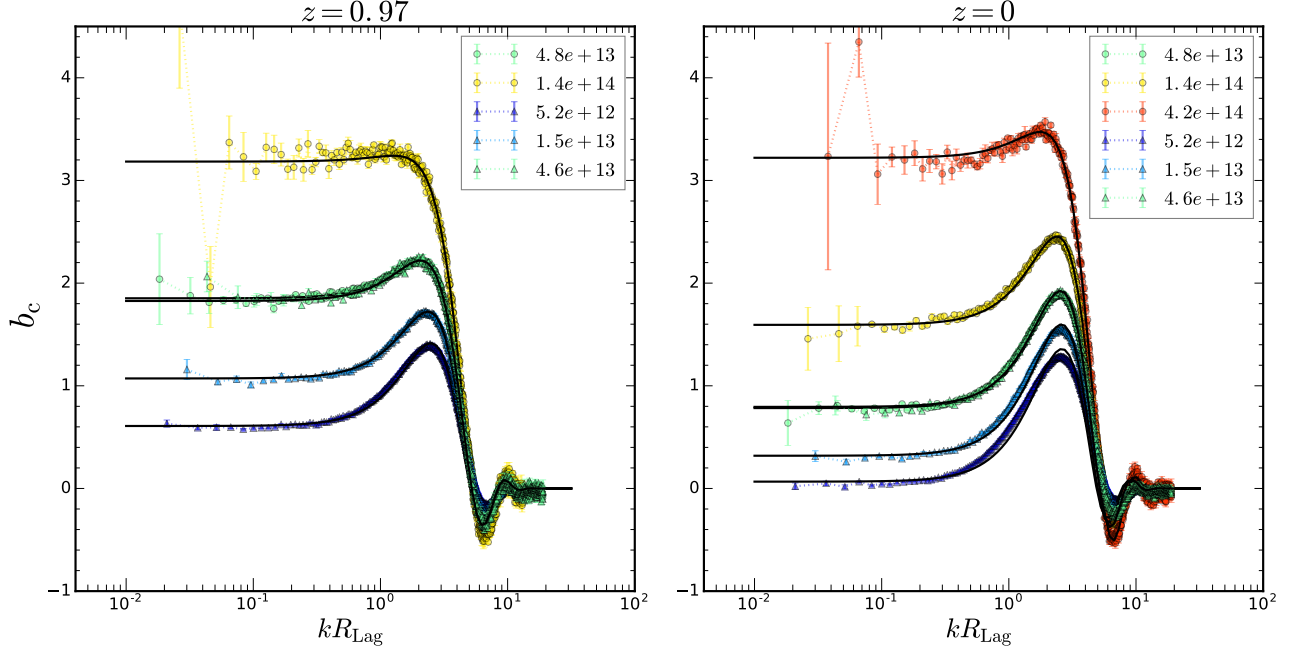


FIG. 4: Lagrangian cross bias parameter b_c for the Lagrangian protohalos of Eulerian halos at $z = 0.97$ (left) and $z = 0$ (right) in the Oriana (circle) and Carmen (triangle) simulations, for a range of halo masses (legend, in units of $h^{-1}M_\odot$). Solid black curves show the result of fitting Eq. (15) to these measurements with $W = W_{\text{eff}}$ and $f = 1$ in Eq. (6).

protohalo-matter cross bias is [28]

$$b_W(k) = \left[b_{10} + 2b_{01} \frac{d \ln W(k)}{d \ln s_0} \right] W(k), \quad (15)$$

where

$$s_j \equiv \sigma_j^2 = \int \frac{dk}{k} \frac{4\pi k^3}{(2\pi)^3} k^{2j} P_m(k, 0) W^2(kR), \quad (16)$$

$P_m(k, 0)$ is the initial dark matter power spectrum extrapolated using linear theory to $z = 0$, and b_{10} and b_{01} are dimensionless bias parameters whose numerical values depend on protohalo mass (i.e. on R_{Lag}). Our notation highlights the fact that the smoothing window W plays a crucial role.

Typically, $W \rightarrow 1$ as $k \rightarrow 0$. In this limit $b_W(k) \rightarrow b_{10}$, so b_{10} can be estimated reliably with little knowledge of the window. However, the expression above shows that, to measure the bias parameter b_{01} associated with scale dependent bias, one must model W accurately.

A Gaussian smoothing window has long been a popular choice [e.g. 5, 21, 24]. However, the obvious oscillations at large kR_{Lag} in Fig. 3 rule this out as a viable model. In contrast, the bias associated with setting $W = W_{\text{TH}}$ in Eq. (15) will oscillate, though there is no guarantee that the phase or amplitude of the oscillations will match the measurements.

The blue curves show the result of setting $W = W_{\text{TH}}$ and treating b_{10} , b_{01} and R as free parameters when fitting b_W to our measurements. (Because the high- k -part

generally has smaller error bars compared to the low- k -part, to make sure the low- k -part is properly fitted, we first determine b_{10} by fitting to $kR_{\text{Lag}} \leq 0.15$. We then keep this value of b_{10} fixed and fit b_{01} and R over the range $kR_{\text{Lag}} \leq 4$. We do so because although the numerical uncertainty of the low- k -part is relatively large, its theoretical uncertainty is small.) Evidently, the best-fit model over-predicts the amplitude of the oscillations. This suggests that W_{eff} of Eq. (6), a Gaussian smoothed tophat, may be able to provide a better description: the Gaussian term will damp the oscillations.

The red curves show the result of replacing W_{TH} with W_{eff} in Eq. (15). Although this does provide a better description of the measurements, the amplitude of the oscillations in the best-fit model is still too large, especially at low masses. Green curves show the result of allowing f – the parameter which controls the strength of the Gaussian damping – to vary (we also extend the range over which we fit to $kR_{\text{Lag}} \leq 8$). Now the fit is good for all masses, with a hint that the model ceases to provide a good description when $\nu_{\text{sc}} \lesssim 1$. Comparison of the curves shows that W_{TH} provides a good fit up to the peak in b_c , but it fails at larger kR_{Lag} ; on these scales, W_{eff} is much more accurate if f is allowed to vary.

Fig. 4 shows that Eq. (15) with W_{eff} and $f = 1$ fits our measurements well also for the protohalos of halos identified at $z \sim 1$, although, as for $z = 0$ halos, its performance starts to deteriorate when $\nu_{\text{sc}} \lesssim 2$. Since the main focus of this paper is W_{eff} , rather than the values of

the best-fitting parameters themselves, we only provide these values in Appendix A 3. In [29] we show how to use the best-fitting bias parameters, b_{10} and b_{01} , to extract information about the physics of halo formation.

III. EXCURSION SET PEAK MASS FUNCTION USING THE EFFECTIVE WINDOW

The original peak model [5] considered peaks in the overdensity field identified on a fixed smoothing scale. The excursion set approach [3] asserts that, to define protohalos, one must consider multiple smoothing scales. While this multi-scale problem is difficult to handle analytically, the simpler problem, in which one considers one smoothing scale and the derivative on that same scale, is tractable and rather accurate [4]. Refs. [11–13] showed how to merge the two approaches to define the excursion set peak (ESP) model.

The spectral moments s_j play an important role in the ESP approach; Eq. (16) shows that they depend on the shape of the smoothing window. The first derivations of the excursion set peak (ESP) mass function [11, 12] used Gaussian smoothing windows for all s_j . In contrast, [13] used different smoothing windows for different spectral moments – in effect, they used tophat smoothing for the overdensity and its scale dependence (the excursion set constraint) and Gaussian smoothing for spatial dependence (the peak curvature constraint). They also made a well-motivated approximation which derived from the fact that the peak curvature and excursion set variables are tightly correlated. [14] showed that the approximation in [13] differed from the exact expression by only a few percent; however, they too used different smoothing filters for the different s_j . Since our W_{eff} leads to convergent s_j for all j of interest, it is natural to ask: What is the associated ESP mass function? It turns out that using the same smoothing window for all quantities which matter yields an expression which is essentially the same as Eq. (10) of [14], as we describe shortly.

First, we must account for the fact that the ESP predictions also depend on the critical overdensity required for a protohalo to collapse and form a halo. This critical density is expected to vary from one halo to another, with a mean which is close to that associated with the spherical collapse model. However, as noted by [29], the precise value of the mean, and the scatter around it, will both depend on choice of filter. [13, 14] used a tophat filter when smoothing the overdensity field, since this is the filter which is usually assumed in the spherical collapse calculation. Since we use W_{eff} throughout, we must check if the distribution of protohalo overdensities associated with W_{eff} differs from that in previous work.

Fig. 5 shows that there is indeed a difference. The panels on the left and right show the mean overdensity within W_{TH} and W_{eff} for a range of halo masses, here parametrized by ν_{sc} , for which σ_0 is smoothed by W_{TH} or W_{eff} respectively. Comparison of the histograms in

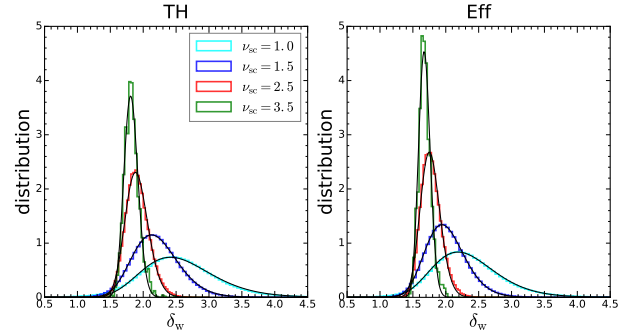


FIG. 5: Distribution of overdensity within protohalo patches for $\nu_{\text{sc}} = 1, 1.5, 2.5$, and 3.5 (histograms), and the corresponding best-fit lognormal distributions (solid black line). Left and right panels show results for W_{TH} and W_{eff} , respectively.

the two panels shows that the mean and variance are slightly smaller for W_{eff} : $\langle \delta_{\text{TH}} \rangle = 1.51 + 0.63\sigma_0$ and $\langle \delta_{\text{eff}} \rangle = 1.42 + 0.55\sigma_0$, with variance $\Sigma_{\text{TH}}^2 = 0.0861\sigma_0^{2.66}$ and $\Sigma_{\text{eff}}^2 = 0.0645\sigma_0^{2.67}$. The difference in the mean is easily understood: the enclosed density is typically a decreasing function of scale, and W_{eff} is more extended than W_{TH} . The solid curves show the best-fitting lognormal distributions. As we describe below, we use these lognormal fits to the measured distributions when generating our ESP mass functions.

A. Halo abundances

The comoving number density of ESP peaks of mass M is

$$n(M) \equiv \frac{\rho_m}{M} \frac{d \ln \nu_{\text{sc}}}{d \ln M} \nu_{\text{sc}} f_{\text{esp}}(\nu_{\text{sc}}). \quad (17)$$

In ν_{sc} , $\sigma_0(R_{\text{Lag}})$ is related monotonically to mass $M \equiv \rho_m 4\pi R_{\text{Lag}}^3/3$, but this relation depends on the shape of the smoothing filter.

The ESP multiplicity function f_{esp} is obtained by averaging its value $f_{\text{esp}}(\nu_{\text{sc}}|\epsilon)$ for a fixed ‘barrier’ of ‘height’

$$B(s_0) = \delta_0 + \epsilon \sqrt{s_0}, \quad (18)$$

over the distribution of heights, here parametrized by a distribution of ϵ :

$$f_{\text{esp}}(\nu_{\text{sc}}) = \int d\epsilon f_{\text{esp}}(\nu_{\text{sc}}|\epsilon) p(\epsilon). \quad (19)$$

I.e., B is the quantity we called δ_W in Fig. 5, and its distribution is attributed to ϵ (rather than δ_0). Note

that our ϵ is β in [13], and our $f_{\text{esp}}(\nu_{\text{sc}}|\epsilon)$ is

$$f_{\text{esp}}(\nu_{\text{sc}}|\epsilon) = \frac{M/(\bar{\rho} V_*)}{\gamma_{\nu u} \nu_{\text{sc}}} \frac{e^{-\nu^2/2}}{\sqrt{2\pi}} \times \int_0^\infty dx f(x) \frac{e^{-(x-\gamma_{x\nu}\nu)^2/[2(1-\gamma_{x\nu}^2)]}}{\sqrt{2\pi(1-\gamma_{x\nu}^2)}} \times \int_{u_0}^\infty du (u-u_0) p(u|\nu, x), \quad (20)$$

where $\nu = B/\sigma_0 = (\delta_0/\delta_{\text{sc}})\nu_{\text{sc}} + \epsilon$ is the peak height variable in units of its rms on scale R_{Lag} , $x \equiv -\nabla^2\delta/\sqrt{s_2}$ is the peak curvature variable in units of its rms on scale R_{Lag} , $u_0 \equiv (dB/ds_0)/\sigma_u$ is the excursion set variable in units of its rms $\sigma_u \equiv \langle (d\delta/ds_0)^2 \rangle^{1/2}$, evaluated at $s_0(R_{\text{Lag}})$, $V_* \equiv (6\pi s_1/s_2)^{3/2}$, and $f(x)$ is given by Eq.(A15) of [5]. Here $\gamma_{\nu u} = (2\sigma_u\sigma_0)^{-1}$ and $\gamma_{x\nu} = s_1/(\sigma_0\sigma_2)$ are the normalized cross-correlation coefficients between δ and u , and δ and x , respectively. The distribution $p(u|\nu, x)$ is a conditional Gaussian distribution, so the integral over u yields

$$\bar{u} \left[\frac{1 + \text{erf}(\bar{u}/(\sqrt{2}\Sigma))}{2} + \frac{\Sigma}{\bar{u}} \frac{e^{-\bar{u}^2/(2\Sigma^2)}}{\sqrt{2\pi}} \right], \quad (21)$$

where

$$\bar{u} \equiv x \frac{\gamma_{xu} - \gamma_{x\nu}\gamma_{\nu u}}{1 - \gamma_{\nu x}^2} + \nu \frac{\gamma_{\nu u} - \gamma_{\nu x}\gamma_{xu}}{1 - \gamma_{\nu x}^2} - u_0, \quad (22)$$

and

$$\Sigma^2 = \frac{1 - \gamma_{\nu x}^2 - \gamma_{\nu u}^2 - \gamma_{xu}^2 + 2\gamma_{\nu x}\gamma_{\nu u}\gamma_{xu}}{1 - \gamma_{\nu x}^2}. \quad (23)$$

(As our notation suggests, γ_{xu} denotes the cross correlation coefficient between x and u).

Our Eq. (19) is the same as Eq. (10) of [14], except that our ϵ and x are their β and u , our u is proportional to their $-\mu$ (to conform with more standard notation), we are more careful about the limits of integration on our u (this gives the extra u_0 term in \bar{u}), our Σ^2 corrects what appears to be a typographical error in their Eq. (14), and we use the same smoothing window, W_{eff} , in all the expressions for covariances between variables (e.g., their Eqs. 3–5 and 10). Eq. (14) of [13] approximates $p(u|\nu, x)$ as a delta function centered on x (for Gaussian smoothing $\gamma_{xu} = 1$ and $\gamma_{\nu x} = \gamma_{\nu u}$), and uses Tophat smoothing for δ but Gaussian smoothing for x , with $R_G \approx R_{\text{TH}}/\sqrt{5}$ (which comes from matching $W_{\text{TH}}(x)$ and $W_G(x)$ to order x^2).

The symbols in Fig. 6 show the $z = 0$ mass function measured in the simulations: triangles and circles represent Carmen and Oriana. The curves in the top panel show the ESP prediction, Eq. (19), with three different pairings of the smoothing window and the critical overdensity. The solid blue curve uses W_{TH} for δ but W_G for x , so we loosely refer to it as having ‘mixed’ smoothing, W_{mix} . Since δ is smoothed with a tophat, we use

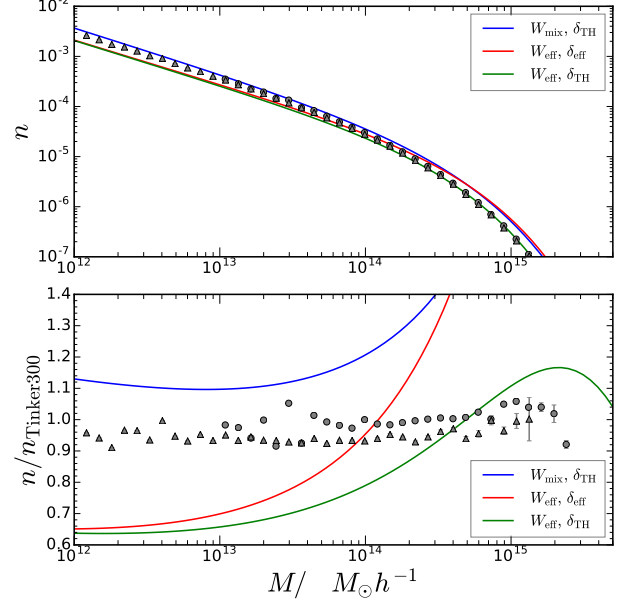


FIG. 6: Top: The $z = 0$ mass function n measured in simulations (triangles for Carmen, circles for Oriana). Curves show three ESP predictions as labeled in the legend. Bottom: Mass functions normalized by the fitting formula from Ref. [37] for halos having spherical overdensity $\Delta = 300$.

our fits to the distributions shown in the left hand panel of Fig 5 for the associated critical overdensity. The red curve uses W_{eff} , so the critical overdensity comes from fitting to the results shown in the right hand panel of Fig 5. The green curve uses W_{eff} but δ_{TH} as a crude way of accounting for the fact that W_{eff} does not select a random subset of particles, but the subset with larger infall speeds (c.f. Appendix C).

To reduce the dynamic range, the lower panel shows the mass function normalized by the fitting formula of Ref. [37] for the abundance of spherical overdensity halos identified because they are $\Delta = 300$ times denser than the background. This formula is similar to that of Ref. [38]. This format makes it easy to see that the W_{mix} prescription works reasonably well at smaller masses, though the agreement is not quite as good as demonstrated by Ref. [13] for $\Delta = 200$ SO halos. However, it overpredicts the counts at larger masses. Our W_{eff} also overpredicts at large masses, but underpredicts by nearly a factor of 2 at smaller masses. Using $\delta_{\text{eff}} \rightarrow \delta_{\text{TH}}$ with W_{eff} produces good agreement at large masses, but does not fix the problem at smaller masses.

B. Lagrangian protohalo bias

We remarked in the Introduction that there is a tight connection between halo abundances and clustering. So, having compared ESP mass functions for W_{eff} and W_{mix} ,

we now discuss their associated ESP bias factors.

In the ESP approach, protohalo patches satisfy three constraints: their enclosed density must be large enough; this density must be larger than that on the next larger smoothing scale (the ES in ESP); and it must be a local peak (the P in ESP). Therefore, b_c is expected to be the sum of three terms, each having slightly different k -dependence: the first scales as W , the second as $dW/d\ln s_0$, and the third as k^2W . For a Gaussian smoothing filter, the latter two are exactly degenerate. For more general filters, it would be reasonable to expect that one can model b_c quite accurately by using W and either $dW/d\ln s_0$ or $(kR)^2W$, but it may not be necessary to use both [29]. The model fits in Figs. 3 and 4 show that this indeed seems to be the case for W_{eff} ; Eq. (15), which does not have a $(kR)^2W$ term, provides a good description of the measurements.

However, this is not as straightforward for W_{mix} , since the approach uses W_{TH} , $dW_{\text{TH}}/d\ln s_0^{\text{TH}}$ and $(kR_{\text{G}})^2W_{\text{G}}$ with $R_{\text{G}} = R_{\text{TH}}/\sqrt{5}$. In this case, the $kR \gg 1$ dependence of W_{TH} is very different from that of W_{G} . The blue curves in Fig. 3 show that Eq. (15) with W_{TH} is a bad choice; its oscillations at large kR_{TH} are too strong. In addition, that there are oscillations at all mean that using W_{G} in Eq. (15) will not work either. Finally, approximating

$$b_{\text{mix}}(k) = b_{10}^{\text{mix}} W_{\text{TH}}(kR_{\text{TH}}) + b_{01}^{\text{mix}} \frac{s_0^{\text{TH}}}{s_1^{\text{mix}}} k^2 W_{\text{G}} \left(\frac{kR_{\text{TH}}}{\sqrt{5}} \right), \quad (24)$$

where s_1^{mix} is given by Eq. (16), but with $W^2 \rightarrow W_{\text{TH}}W_{\text{G}}$ is not accurate either; because there is no oscillations in W_{G} , the wiggles from the b_{10} -term is too weak compared to the numerical results.

Ref. [29] suggest that one might define linear combinations of the $dW/d\ln s_0$ and k^2W contributions – a suitably weighted sum, T_+ , and difference, T_- , of the two terms. (The idea is that T_- should only matter at larger kR_{Lag} .) Although we do not show it here, we have found that using only W_{TH} and T_+^{mix} still leads to unacceptably large oscillations at large kR_{Lag} . We conclude that although the W_{mix} -based approach provides a slightly better description of halo abundances, our W_{eff} -approach provides a more efficient description of Lagrangian protohalo bias.

IV. CONCLUSIONS

It is often assumed that protohalos in the initial conditions can be defined using a spherical tophat window function. This is, of course an idealization. Other than being a convenient approximation in the context of the spherical collapse model, there is no fundamental reason why the protohalo profile should be a spherical tophat. Realistically, we expect some particles within the Lagrangian protohalo patch – those with insufficiently large infall speeds – will not be incorporated into the final ob-

ject, while others which were initially more distant may be, provided they fell in quickly enough. Thus we expect that, if the protohalo particles are those whose infall times are smaller than the present time, then the spatial distribution of the spherically averaged protohalo profile will be more extended than a tophat (Appendix C).

We explored this issue by measuring the Lagrangian protohalo profile in numerical simulations. We did so by identifying halos of similar masses, stacking their protohalo patches together, and measuring the spherically averaged profile of the stack. We found that the Lagrangian protohalo profile is indeed more extended than a tophat, but less extended than a Gaussian (Fig. 1). In Fourier space, the profile W_{eff} is well approximated by the product of a tophat and a Gaussian (Eq. (6)). The convolution which describes the real space profile can be done analytically (Eq. (8)) so most analyses of halo abundances and clustering, which assume tophat or Gaussian profiles, can be performed with little modification.

For example, in excursion set approaches, the protohalo-matter cross power spectrum is the product of a scale-dependent bias factor and the window function (Eq. (15)). Since the two effects appear combined in any measurement, to measure the scale-dependence of bias, the window function must be modeled accurately. We find that using W_{eff} of Eq. (6) in Eq. (15) describes the measured cross spectrum well up to $kR_{\text{Lag}} \sim 10$ (Figs. 3 and 4). Importantly, the same window function also describes the protohalo profile in real space (Fig. 1).

In the excursion set peak approach, predicting the abundance and clustering of halos requires the evaluation of the spectral moments in Eq. (16). Some of these integrals diverge for a tophat filter, and this complicates how the approach is implemented. In contrast, they are all well defined for our W_{eff} , so this allows a more straightforward ESP analysis (Sec. III). The predicted mass functions also depend on the critical threshold overdensity required for collapse. We use the values measured in the simulations (Fig. 5), leaving no free parameters. The predicted ESP mass function, Eq. (19), is not more accurate than the old mixed-filtering prediction; it significantly underpredicts the counts at lower masses (Fig. 6). On the other hand, using the critical overdensity associated with tophat smoothing results in better agreement, especially at high masses. This suggests that a more fully Lagrangian model, built on infall speeds rather than smoothed overdensity, may be more realistic (Appendix C 2) and ultimately more accurate.

On the other hand, our W_{eff} approach does provide a better description of the scale dependence of bias, which it describes to $kR_{\text{Lag}} \gg 1$ for halos with $\nu_{\text{sc}} \geq 1$. The accuracy of our estimated bias parameters allows us to check the consistency relations that these bias parameters should satisfy [13, 28]. In [29], we show that this accuracy allows us to extract information about physics of halo formation from measurements of the large-scale bias.

Acknowledgments

We thank A. Paranjape for insightful discussions, V. Desjacques for comments on an early draft of the paper, and the anonymous referee for constructive comments that improved the paper. We acknowledge the LasDamas project¹ for the simulations used in this work, which were run using a Teragrid allocation as well as other RPI and NYU computing resources. KCC thanks the ICTP in Trieste and the theory group of CERN, where part of the work was done, for their hospitality, and acknowledges support from the Swiss National Science Foundation and the Spanish Ministerio de Economía y Competitividad grant ESP2013-48274-C3-1-P.

Appendix A: Systematic effects

1. Discreteness of the Lagrangian grid

Fig. 7 compares $p_h = n_h/n_m$ values for halos in the same narrow mass bin in the Carmen (triangles, about 670 particles) and Oriana (circles, about 66 particles) simulations. The blue symbols estimate both n_h and n_m from the particle distribution in the simulations, as we do in the main text. The red symbols use the mean particle density \bar{n}_m for the denominator n_m . This continuous approximation is noisy, especially for the first bin shown. The red circles drop dramatically at small $r/R_{\text{Lag}} \leq 0.2$; discreteness effects clearly compromise these estimates in the lower resolution halo. On these scales, the blue circles lie well above the red circles, indicating that the estimator which uses the actual particles performs better. On the other hand, the blue circles lie slightly below the triangles: even with this estimator, discreteness is still an issue for the low resolution simulation. In contrast, the red and blue triangles are rather similar: discreteness is not an issue for the higher resolution halo. We conclude that some of the offsets of p_h from unity at small r are systematics and not physical.

In the main text, we used the parameter A to account for the fact that p_h did not asymptote to unity at small r . If some of the departures from unity which we show in Fig. 2 are systematics associated with discreteness, then we expect them to scale with protohalo mass. Fig. 8 shows those results as a function of M rather than ν_{sc} . At fixed M and z , we do not see strong differences between the two simulation sets. Moreover, the dependence on z is reduced when shown as a function of ν_{sc} (as in the main text). Thus, Fig. 8 suggests that most of the tendency for higher ν_{sc} to have larger A is real. This may be related to the fact that small ν protohalos tend to be less spherical.

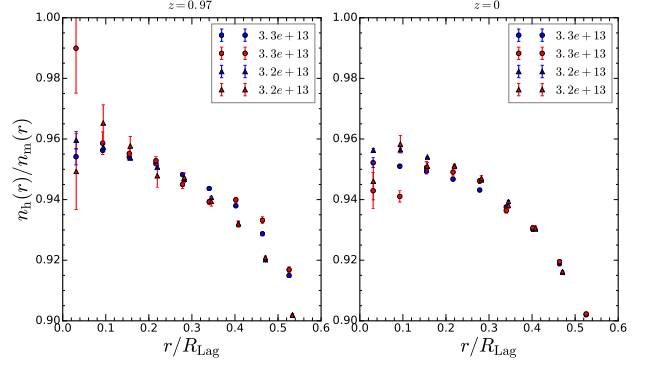


FIG. 7: Comparison of $p_h = n_h/n_m$ values for protohalos in the same narrow mass bin (legend gives masses in units of $h^{-1}M_\odot$) in the Carmen (triangles) and Oriana (circles) simulations. Each Carmen halo has about 670 particles, and this is about $10\times$ that in each Oriana halo. Red symbols use the mean particle density \bar{n}_m for the denominator n_m ; blue symbols show when both n_h and n_m are measured in the simulations. At small $r/R_{\text{Lag}} \leq 0.2$, the red circles indicate smaller p_h than the blue circles, which themselves lie below the triangles: on these scales the discreteness of the grid has compromised the estimate of p_h for the low resolution protohalo.

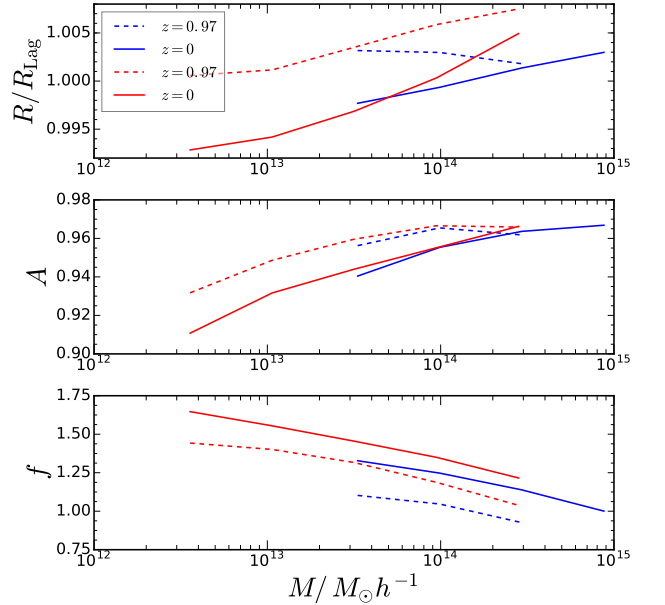


FIG. 8: Same as Fig. 2, except that the best-fit parameters ρ , A and f for the Lagrangian protohalos are now shown as a function of halo mass. Red and blue curves show results for $z = 0.97$ (dashed) and $z = 0$ (solid) protohalos in the high and low resolution simulations (Carmen and Oriana).

¹ <http://lss.phy.vanderbilt.edu/lasdamas>

2. Estimating the Lagrangian window from the displaced field

We now discuss a method which uses the displaced particles to estimate p_h . As we mentioned in Sec. II A, in this case we cannot replace n_m by \bar{n}_m . Due to the presence of the halo at the origin, we must set

$$n_m(r) = \bar{n}_m[1 + \xi_c(r)], \quad (\text{A1})$$

where ξ_c is the cross correlation function between halo and matter. We can either measure ξ_c directly or model it. To model ξ_c we use the bias model Eq. (15) given together with the bias parameters computed from the peak model [13] to obtain the cross power spectrum. Then ξ_c follows after an inverse Fourier transform. As in this paper, we focus on the window function, we will present the details of the model and the comparison with numerical measurements elsewhere [29]. We find that the model we adopted describes the simulation data well. Hence we will use ξ_c obtained from theory here. In Fig. 9, we compare the measurement n_h^d/\bar{n}_m and $(n_h^d/\bar{n}_m)/(1+\xi_c)$, where the superscript d in n_h^d emphasizes that it is estimated using the displaced particle distribution. We have used the Lagrangian halos at $z=0$ from the Carmen simulation in this plot. The clustering correction is mainly important for $r \lesssim R_{\text{Lag}}$, while for larger r , $\xi_c \ll 1$. Due to the clustering enhancement, n_h^d/\bar{n}_m exceeds 1 for $r/R_{\text{Lag}} \lesssim 0.5$. After the correction, we find that the results agree with those from the method described in the main text very well (right panel of Fig. 1). This method is interesting in its own right: That we are able to correct for the clustering effect is a non-trivial consistency check of our approach.

The main text used the initial Gaussian random field to compute the cross power spectrum. It is worth pointing out how b_c in Fourier space changes when the evolved dark matter field is used instead. Fig. 10 compares b_c obtained using the initial Gaussian random field (triangles) with that for the 2LPT particle distribution (circles). At low k , these two cases coincide as we do not expect this evolution to modify the b_{01} -part although the one from the particle distribution is slightly noisier. Both cases show similar oscillatory patterns. However, deviations arise around $kR_{\text{Lag}} \sim 2$, where b_c from the evolved field is slightly larger.

Figs. 9 and 10 demonstrate that the evolution of the dark matter field does not change the large scale, but the small scale ($r/R_{\text{Lag}} \lesssim 1$ or $kR_{\text{Lag}} \gtrsim 1$) is enhanced by evolution.

3. Best-fitting cross-bias parameters

The main text shows that W_{eff} , together with the excursion set bias model, provides a better description of the protohalo-matter cross bias parameter than does a tophat window W_{TH} .

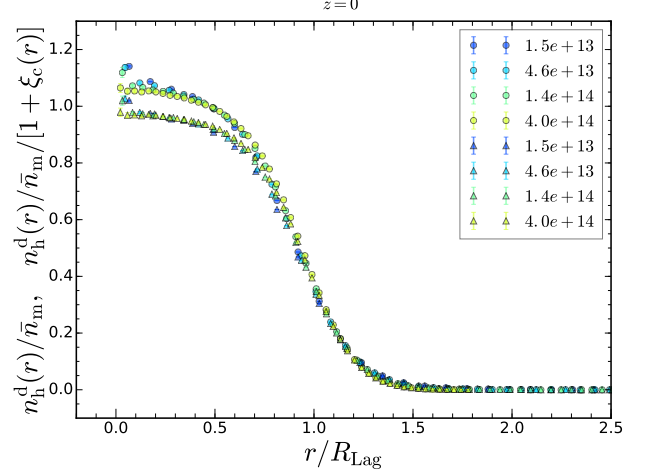


FIG. 9: The ratio n_h^d/\bar{n}_m obtained using displaced particles at the initial redshift $z_* = 49$ (circles, the upper set of curves) and when the clustering effect has been corrected $(n_h/\bar{n}_m)/(1+\xi_c)$ (triangles, the lower set). Results are for the Lagrangian protohalos of the $z=0$ halos in the higher resolution (Carmen) simulations; legend gives the mean mass of each sample in units of $h^{-1}M_\odot$.

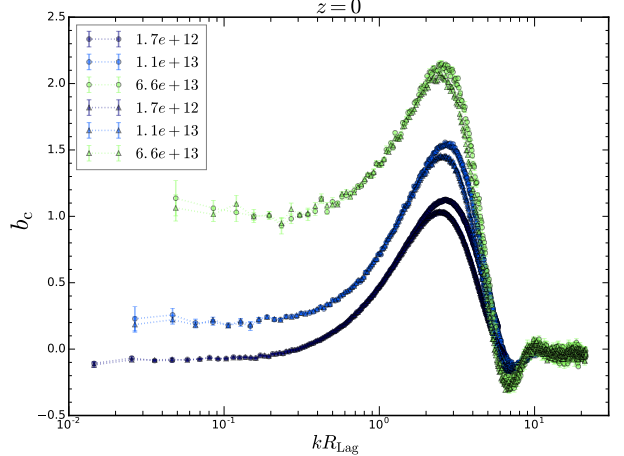


FIG. 10: Lagrangian bias b_c obtained by cross correlating the Lagrangian halo field with the initial Gaussian random field (triangles) and the 2LPT particle distribution field (circles) for a range of protohalo masses (legend gives masses in units of $h^{-1}M_\odot$) for the $z=0$ halos in the higher resolution (Carmen) simulations.

Fig. 11 shows the best fit parameters for these fits. When f is set to unity, and only b_{10} , b_{01} and R are varied, then we only attempt to fit to the measurements at $kR_{\text{Lag}} \leq 4$; when f is also varied, then we fit up to $kR_{\text{Lag}} \leq 8$. As we noted in the main text, b_{10} is insensitive to the window function adopted, and this is especially true for our fitting procedure. For b_{01} , the two W_{eff} fits (i.e. with $f=1$ and variable f) yield similar results,

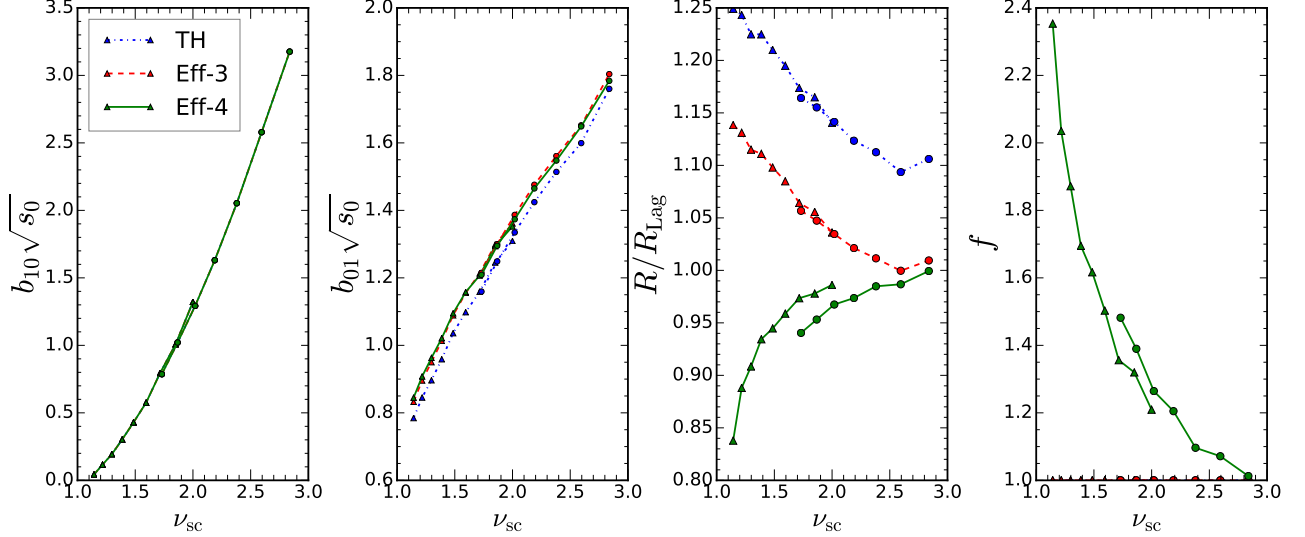


FIG. 11: The best fit parameters b_{10} , b_{01} , R and f determined from fitting Eq. (15) to the protohalo-matter cross correlation measurements shown in Fig. 3. Dotted blue and dashed red lines show results associated with W_{TH} and W_{eff} when $f = 1$; solid green uses W_{eff} and allows f to also vary. The measurements are from Oriana (circles) and Carmen (triangles) at $z = 0$.

while the value associated with W_{TH} is slightly lower.

For W_{TH} , the best-fit R is larger than R_{Lag} by at least 10%. For W_{eff} , R agrees with R_{Lag} for $\nu_{\text{sc}} \gtrsim 2.5$, but it too exceeds R_{Lag} as ν_{sc} decreases. This can be understood as follows. As ν_{sc} decreases, higher damping is required (e.g. Fig. 3). If f is fixed to unity, then $R_{\text{G}} = R_{\text{TH}}/5$ so this damping can only be incorporated by increasing R_{TH} . When f is allowed to vary, we find it becomes substantially larger than unity, meaning R_{G} can increase so R_{TH} no longer needs be large. (In fact, we actually find that R_{TH} becomes slightly smaller than R_{Lag} at small masses.) Whereas the increase of f at small masses is similar to that in Fig. 2 of the main text, the decrease in R here is larger than that in Fig. 2, perhaps because the parameter A absorbs some of the effect there.

Appendix B: Dependence on halo finder

1. FoF linking length

The main text presented results using halos obtained with linking length $\ell = 0.156$ times the interparticle separation. Here we study how the Lagrangian profile $p_{\text{h}}(r)$ depends on ℓ , by comparing with results for $\ell = 0.2$.

Fig. 12 compares the protohalo profiles of objects identified in the $z = 0$ outputs of the Carmen simulation using $\ell = 0.15$ and $\ell = 0.2$. In both cases, we have chosen objects having mass $\sim 9.4 \times 10^{13} h^{-1} M_{\odot}$ for which discreteness effects should not be an issue. The objects identified using larger ℓ have profiles which are slightly more tophat-like, and which are slightly closer to unity

at small r . While this trend mimics the dependence on halo mass seen at fixed ℓ , one should bear in mind that the $\ell = 0.2$ objects would have had smaller masses in the $\ell = 0.156$ catalog.

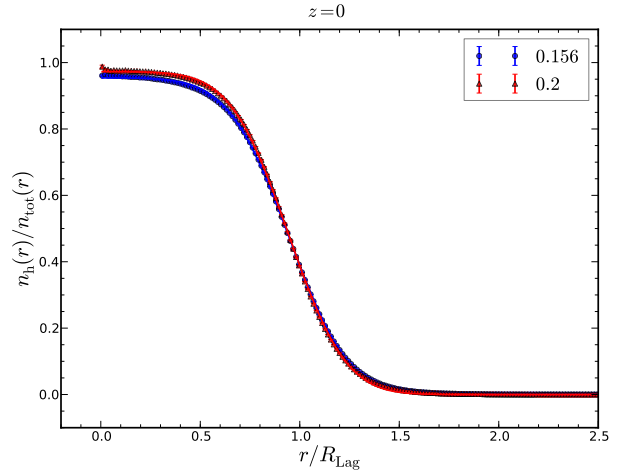


FIG. 12: Lagrangian protohalo profiles of Eulerian halos identified with FoF link lengths $\ell = 0.156$ (blue circles) and 0.2 (red triangles). Both sets of profiles are for halos having mass $\sim 9.4 \times 10^{13} h^{-1} M_{\odot}$, so the values of R_{Lag} are the same, but the objects themselves are not.

We now select the samples such that we are comparing the same halos. We search the $\ell = 0.2$ halos and select those that match the center of mass positions of $\ell = 0.156$ halos. For the $\ell = 0.156$ halos with masses $\sim 9.6 \times 10^{13} h^{-1} M_{\odot}$, the corresponding $\ell = 0.2$ halos have

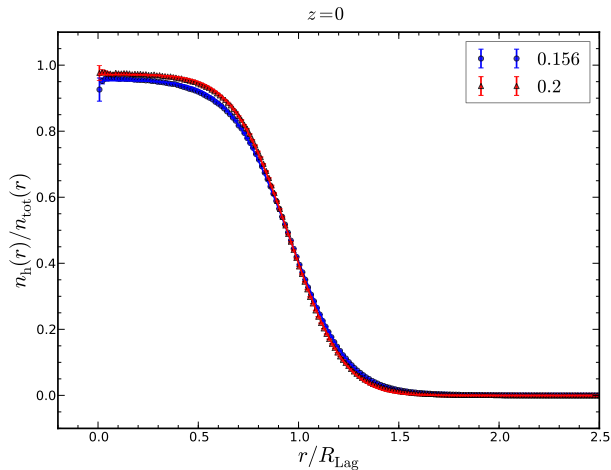


FIG. 13: Similar to Fig. 12 except in this plot, the samples are chosen such that the halos are the same in both cases. However, the $\ell = 0.156$ halo masses are $\sim 9.6 \times 10^{13} h^{-1} M_{\odot}$, while the $\ell = 0.2$ masses are $1.1 \times 10^{14} h^{-1} M_{\odot}$, so the values of R_{Lag} differ by factor of about 1.06.

masses that are about 20% larger: $\sim 1.1 \times 10^{14} h^{-1} M_{\odot}$. Fig. 13 compares their profiles, scaled by their respective R_{Lag} values (which differ by factor of about 1.06). The results are very similar to those in Fig. 12: larger ℓ results in a more compact protohalo profile. Note that, had we rescaled both profiles by the same factor, say R_{Lag} of the $\ell = 0.156$ masses, then the profiles would mainly have differed at small r , with the larger ℓ having larger p_h . This suggests that the difference from unity at small r is real: these are particles which were initially close to the protohalo center, but received large virial kicks, so in the $z = 0$ snapshot they happen to lie beyond the boundary identified by the smaller linking length.

2. FoF vs SO halo finder

The main text used halos identified using an FoF halo finder with $\ell = 0.156$. Here we compare with results based on spherical overdensity (SO) halos that are $200\times$ the critical density and were identified using the public halo finder AHF [39, 40].

Fig. 14 shows p_h obtained from the $\ell = 0.156$ FoF (circles) and SO (triangles) halos identified at $z = 0$ in the Carmen simulations having masses of $9.4 \times 10^{13} h^{-1} M_{\odot}$. At small r , the SO profile has noticeably smaller p_h than the FoF one, suggesting that the nonspherical shapes which FoF allows permit one to identify a greater fraction of the particles that are bound to the halo. However, this is redshift-dependent. At $z = 0.97$, the average SO protohalo profile is slightly more compact than the FoF one. The smooth curves show that, like FoF protohalos, the SO protohalo profiles are also well fitted by our Eq. (8).

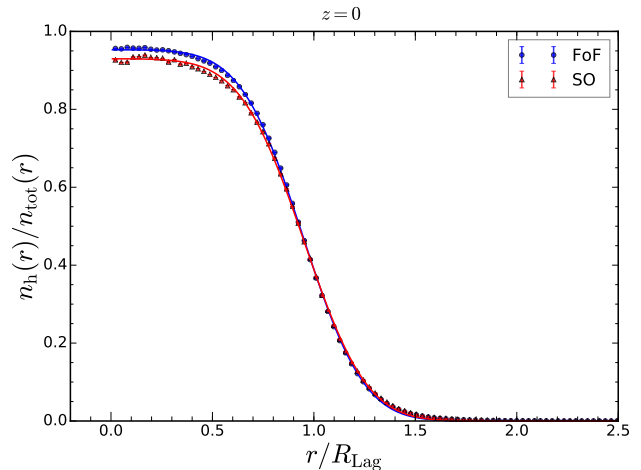


FIG. 14: Lagrangian halo profile obtained from $\ell = 0.156$ FoF (blue circles) and $200\rho_c$ SO (red triangles) halos identified at $z = 0$ in the Carmen simulations. Both FoF and SO masses are $\sim 9.4 \times 10^{13} h^{-1} M_{\odot}$. Smooth curves show the result of fitting Eq. (8) to these profiles.

Appendix C: Relation to spherical collapse and the collapse threshold measurements

Conceptually, going beyond the tophat shape is subtle. This is because the window function plays two roles. In theory calculations, it smooths the initial overdensity field. In the other, which is close to the way measurements are made, it is a weighting function which selects a fraction of the local dark matter particles that go on to become members of the Eulerian halo later on. For a tophat, with a deterministic relation between particle motions and distance from the center, these two roles appear to be the same, but for other filters, or when there is some stochasticity, they need not be. This has two implications, which we use the excursion set approach to illustrate.

1. Smoothing window versus density profile

In the main text, $p(r)$ was obtained using the particle distribution. Therefore, it is tempting to associate it with a density profile, and hence to ask how well the spherical evolution model describes its evolution. We now argue that, in this respect, it really is better to think of this distribution as a smoothing window, W_{eff} , and not as a profile.

Specifically, it is tempting to define the mean overdensity inside r as

$$\bar{\eta}(\leq r) = \frac{3 \int_0^r dr' r'^2 n_h(r')}{r^3 \bar{n}_m} - 1. \quad (\text{C1})$$

However, since $n_h = p_h \bar{n}_m$ and $p_h \leq 1$, the quantity above is guaranteed to be negative. Therefore, if we were

to use this $\bar{\eta}$ as a proxy for overdensity in the spherical evolution model, we would conclude that the protohalo patch would not shrink and collapse (in comoving coordinates). This is a wrong answer, of course, since the particles were identified precisely because they did form a collapsed object.

The error arises because the argument above does not account for the fact that the particles coming from further away must have had higher infall velocities, and the naive application of the spherical model argument has ignored this. It is straightforward to include the fact that the initial velocities are perturbed from the initial Hubble flow in the spherical model analysis. But instead of doing so directly, we think the discussion which follows makes a similar point.

First, define

$$\bar{\delta}_{\text{Lag}} = \int d\mathbf{x}' \delta_{\text{m}}(\mathbf{x}') W_{\text{eff}}(\mathbf{x}'). \quad (\text{C2})$$

This expression represents a smoothing of the initial overdensity fluctuation field centered on the origin (in this case, the center of the protohalo patch). However, the continuity equation relates the overdensity to the divergence of the velocities: so the average over δ_{m} above is like averaging over the velocity divergence. It is this smoothed overdensity which should be inserted into the spherical evolution model. In this respect, $W_{\text{eff}} \leq 1$ in the expression above is a simple way to account for the fact that some particles fall onto the protohalo center and others escape; i.e., it is the motions, the displacements from the initial positions, which matter. The role of W_{eff} is to only count those particles in the initial conditions whose displacements will bring them into the final collapsed object. It does not do this exactly, because the particles which do end up in the final object did not have the average infall speeds, whereas the expression above is assuming they did. If the distribution around the mean is narrow, this will be a good approximation; otherwise, we expect $\bar{\delta}_{\text{Lag}}$ to underestimate the true effective overdensity. This is what motivates the last of our three choices in Fig. 6: whereas using δ_{TH} with W_{TH} and δ_{eff} with W_{eff} are natural choices, using δ_{TH} with W_{eff} is a crude way of accounting for the fact that if W_{eff} is picking out the particles with the largest infall speeds, then their associated effective overdensity will be larger than δ_{eff} .

Previous work has shown that not only is $\bar{\delta}_{\text{Lag}}$ greater than zero, but when a tophat smoothing window is used, then $\bar{\delta}_{\text{Lag}} \geq \delta_{\text{sc}}$ [22, 41]. Therefore, we expect it will also be of order δ_{sc} when W_{eff} is used, and indeed it is (see [29] and Fig. 5). This is the sense in which W_{eff} can be thought of as playing two distinct roles: it is both a fraction of particles, and a smoothing filter which should be applied to the Lagrangian overdensity fluctuation field.

The analysis above suggests that protohalo particles are those for which $v/fHr \sim \delta_{\text{sc}}/3$, a point we flesh out in slightly more detail in the next subsection.

2. Infall speeds and protohalo patches

In the idealized spherical collapse calculation, the initial protohalo is a tophat, with a deterministic relation between particle motions and distance from the center. As a result, the requirement that the particles fall towards the protohalo center of mass and arrive there by the present time, and the requirement that the enclosed density within the patch have a certain critical value, are the same. In reality, things are more complicated.

To see why, suppose that we are centered on a patch in Lagrangian space around which the overdensity, smoothed with a tophat of radius R , equals δ_c , and that the overdensity on the next larger smoothing scale is less than this. If we average over many such patches, we can define the mean overdensity as a function of distance r from the center. The Fourier transform of $\langle \delta(\leq r) | \delta_0, \delta'_0 \rangle$, the average overdensity within r , is the quantity which played a major role in the main text (although here the smoothing filter is obviously W_{TH}). Our notation reflects the fact that the value of δ and its derivative at the origin are constrained.

Similarly, at each r , there will be a distribution of radial infall speeds. Let $p(v_r | \delta_0, \delta'_0)$ denote this distribution. If the initial fluctuation field was Gaussian, then this distribution is Gaussian with a mean $\langle v_r | \delta_0, \delta'_0 \rangle = fHr \langle \delta(\leq r) | \delta_0, \delta'_0 \rangle / 3$ which depends on the value of the constraints, and a variance $\sigma^2(v_r | \delta_0, \delta'_0)$ whose value depends on the fact that the enclosed overdensity and its slope were constraints, but does not depend on δ_0 and δ'_0 themselves.

The particles which will end up in the final halo are those with sufficiently large radial infall speeds. At each r , this is the fraction

$$p(r) = \int_{v(r)}^{\infty} dv_r p(v_r | \delta_0, \delta'_0) \quad (\text{C3})$$

where $v(r) \sim fH(r - r_{\text{vir}}) \sim fH(r - R_{\text{Lag}}/5)$. Clearly, the more distant particles must have larger infall speeds so as to arrive within r_{vir} by the present time. E.g., in the Zeldovich approximation,

$$p(r) = \frac{1}{2} \text{erfc} \left(\frac{r - r_{\text{vir}} - r \langle \delta(\leq r) | \delta_0, \delta'_0 \rangle / 3}{\sqrt{2} \sigma_v | \delta, \delta' / H} \right), \quad (\text{C4})$$

so that

$$p(R_{\text{Lag}}) = \frac{1}{2} \text{erfc} \left(\frac{4/5 - \delta_c/3}{\sqrt{2} \sigma_v | \delta, \delta' / fH R_{\text{Lag}}} \right) \sim 1/2. \quad (\text{C5})$$

But at $r \gg R_{\text{Lag}}$, the term in brackets tends to fHr/σ_v so $p(r) \rightarrow 0$. This shows that: even if δ_0 was identified using a real space tophat of scale R_{Lag} , not all the particles within R_{Lag} will make it into the final halo; and some of the particles which are initially beyond R_{Lag} will end up in the final halo. As a result, $p(r)$ will be more extended than a tophat, in qualitative agreement with

what we found in the main text. I.e., in this picture, one thinks of protohalo particles as those which satisfy a tophat in ‘infall time’ towards the protohalo center, and

this need *not* correspond to a tophat in the initial spatial distribution.

-
- [1] W. H. Press and P. Schechter, *ApJ* **187**, 425 (1974).
 - [2] R. K. Sheth and G. Tormen, *MNRAS* **308**, 119 (1999).
 - [3] J. R. Bond, S. Cole, G. Efstathiou, and N. Kaiser, *ApJ* **379**, 440 (1991).
 - [4] M. Musso and R. K. Sheth, *MNRAS* **423**, L102 (2012).
 - [5] J. M. Bardeen, J. R. Bond, N. Kaiser, and A. S. Szalay, *ApJ* **304**, 15 (1986).
 - [6] J. R. Bond and S. T. Myers, *ApJS* **103**, 1 (1996).
 - [7] V. Desjacques, *Phys. Rev. D* **78**, 103503 (2008), arXiv:0806.0007.
 - [8] V. Desjacques and R. K. Sheth, *Phys. Rev. D* **81**, 023526 (2010), arXiv:0909.4544.
 - [9] V. Desjacques, M. Crocce, R. Scoccimarro, and R. K. Sheth, *Phys. Rev. D* **82**, 103529 (2010), arXiv:1009.3449.
 - [10] V. Desjacques, *Phys. Rev. D* **87**, 043505 (2013), arXiv:1211.4128.
 - [11] L. Appel and B. J. T. Jones, *MNRAS* **245**, 522 (1990).
 - [12] A. Paranjape and R. K. Sheth, *MNRAS* **426**, 2789 (2012).
 - [13] A. Paranjape, R. K. Sheth, and V. Desjacques, *MNRAS* **431**, 1503 (2013), arXiv:1210.1483.
 - [14] M. Biagetti, K. C. Chan, V. Desjacques, and A. Paranjape, *MNRAS* **441**, 1457 (2014).
 - [15] J. E. Gunn and J. R. Gott, III, *ApJ* **176**, 1 (1972).
 - [16] P. J. E. Peebles, *The Large-Scale Structure of the Universe* (Princeton University Press, New Jersey, 1980).
 - [17] T. Padmanabhan, *Structure formation in the Universe* (Cambridge University Press, Cambridge, 1993).
 - [18] D. Lynden-Bell, *MNRAS* **136**, 101 (1967).
 - [19] C. Porciani, A. Dekel, and Y. Hoffman, *MNRAS* **332**, 339 (2002).
 - [20] N. Dalal, M. White, J. R. Bond, and A. Shirokov, *ApJ* **687**, 12 (2008).
 - [21] A. Elia, A. D. Ludlow, and C. Porciani, *MNRAS* **421**, 3472 (2012).
 - [22] G. Despali, G. Tormen, and R. K. Sheth, *MNRAS* **431**, 1143 (2013).
 - [23] T. Baldauf, in *Perturbative approaches to redshift space distortions workshop, Zurich* (2012).
 - [24] T. Baldauf, V. Desjacques, and U. Seljak, *Phys. Rev. D* **92**, 123507 (2015), 1405.5885.
 - [25] K. C. Chan, *Phys. Rev. D* **92**, 123525 (2015), 1507.04753.
 - [26] A. Paranjape, E. Sefusatti, K. C. Chan, V. Desjacques, P. Monaco, and R. K. Sheth, *MNRAS* **436**, 449 (2013).
 - [27] V. Desjacques, D. Jeong, and F. Schmidt, *Large-Scale Galaxy Bias* (2016), 1611.09787.
 - [28] M. Musso, A. Paranjape, and R. K. Sheth, *MNRAS* **427**, 3145 (2012).
 - [29] K. C. Chan, R. K. Sheth, and R. Scoccimarro, *Mon. Not. Roy. Astron. Soc.* **468**, 2232 (2017), 1701.01701.
 - [30] U. Seljak and M. Zaldarriaga, *ApJ* **469**, 437 (1996), arXiv:astro-ph/9603033.
 - [31] M. Crocce, S. Pueblas, and R. Scoccimarro, *MNRAS* **373**, 369 (2006), arXiv:astro-ph/0606505.
 - [32] V. Springel, *MNRAS* **364**, 1105 (2005), arXiv:astro-ph/0505010.
 - [33] M. Davis, G. Efstathiou, C. S. Frenk, and S. D. M. White, *ApJ* **292**, 371 (1985).
 - [34] G. Despali and *et al.*, in preparation (2017).
 - [35] N. Frusciante and R. K. Sheth, *JCAP* **1211**, 016 (2012), arXiv:1208.0229.
 - [36] K. C. Chan, R. Scoccimarro, and R. K. Sheth, *Phys. Rev. D* **85**, 083509 (2012), arXiv:1201.3614.
 - [37] J. Tinker, A. V. Kravtsov, A. Klypin, K. Abazajian, M. Warren, G. Yepes, S. Gottlöber, and D. E. Holz, *ApJ* **688**, 709-728 (2008), 0803.2706.
 - [38] G. Despali, C. Giocoli, R. E. Angulo, G. Tormen, R. K. Sheth, G. Baso, and L. Moscardini, *MNRAS* **456**, 2486 (2016), 1507.05627.
 - [39] S. P. D. Gill, A. Knebe, and B. K. Gibson, *Mon. Not. Roy. Astron. Soc.* **351**, 399 (2004), astro-ph/0404258.
 - [40] S. R. Knollmann and A. Knebe, *Astrophys. J. Suppl.* **182**, 608 (2009), 0904.3662.
 - [41] R. K. Sheth, H. J. Mo, and G. Tormen, *MNRAS* **323**, 1 (2001).